ORIGINAL ARTICLE

Tidal harmonics retrieval using GNSS-R dual-frequency complex observations

Mahmoud Rajabi[1] · Mostafa Hoseini[1] · Hossein Nahavandchi[1] · Milad Asgarimehr[2] · Maximilian Semmling[3] ·
Markus Ramatschi[4] · Mehdi Goli[5] · Jens Wickert[4,6]

Abstract

Tidal analysis and methods for estimation and prediction of ocean tidal constitutes are essential in a large area of scientific disciplines, for example, navigation, onshore and offshore engineering, and production of green energy. Ground-based Global Navigation Satellite System-Reflectometry (GNSS-R) has been proposed as an alternative method for measuring sea surface height. We use 6 years of GNSS-R observations at In-phase and Quadrature levels from July 2015 to May 2021 obtained from a dedicated receiver and sea-looking left hand circular polarization antenna for estimating sea level (SL). In the first step, the multivariate least-square harmonic estimation (LS-HE) method is applied for SL estimation. Then, final SL time series are generated by combining estimated SL from all satellites at L1 and L2 frequencies in the averaging step. The 6-year root-mean-square error between GNSS-R L12 sea surface heights and a collocated tide gauge (TG) is 5.8 cm with a correlation of 0.948 for a high temporal resolution of 5 min with 15 min averaging window. Afterward, using the univariate LS-HE, we detect tidal harmonics with periods between 30 min to 1 year. The detection results highlight a good match between GNSS-R and TG. Higher harmonics, i.e., the periods shorter than 3 h, show stronger signatures in GNSS-R data. Finally, we estimate the amplitude and phase of standard tidal harmonics from the two datasets. The results show an overall good agreement between the datasets with a few exceptions.

Keywords Global Navigation Satellite Systems Reflectometry (GNSS-R) · Tidal analysis · Altimetry · GPS · GNSS · Coastal waters remote sensing · Least-squares harmonic estimation (LS-HE)

1 Introduction

Tides are periodic fluctuations of the sea level due to astronomical objects, for example, sun, moon, and earth rotation

✉   Mahmoud Rajabi
      mahmoud.rajabi@ntnu.no

[1]   Civil and Environmental Engineering, Norwegian University of Science and Technology, 7491 Trondheim, Norway

[2]   German Research Centre for Geosciences (GFZ), 14473 Potsdam, Germany

[3]   German Aerospace Center DLR, Institute for Solar-Terrestrial Physics, Neustrelitz, Germany

[4]   Department of Geodesy, German Research Center for Geosciences (GFZ), 14473 Potsdam, Germany

[5]   Faculty of Civil and Architectural Engineering, Shahrood University of Technology, Shahrood, Iran

[6]   The Institute of Geodesy and Geoinformation Science, Technische Universität, Berlin, Germany

gravity effects (Doodson 1954; Shum et al. 2001; Devlin 2016). Knowledge of the tide is essential for safe ship navigation, coastal engineering, marine pollution management, surveying engineering, marine tourism, and commercial and recreational fishermen. Moreover, tidal energy is on its way to being one of the important sources of clean, reliable, and sustainable energy (Rourke et al. 2010). Sea level has long been an essential parameter for numerous coastal and offshore services, for example, defining national reference level systems, easing port operation, security, and safety, facilitating navigation, and as an important index of climate changes (Adebisi et al. 2021). Besides tide gauge as the main method for sea-level monitoring, satellite altimetry, and Global Navigation Satellite Systems Reflectometry (GNSS-R) have also been used. The history of using tide poles goes back to the 1770 s (Church and White 2011). Tide gauges measure sea level, relative to a local geodetic monument as a reference level. Although tide gauges can obtain precise relative sea level, there are some limitations and challenges, for exam-

ple, vertical land movement (Cipollini et al. 2017), stability of the area, and connecting the relative sea level to a global reference frame. The limitation of satellite altimetry lies primarily in its low repeat period, limiting its ability to capture rapid changes in ocean dynamics. Additionally, it is often restricted in its use near coastlines due to contamination from land reflections. (Marti et al. 2019).

The utilization of the Global Navigation Satellite Systems (GNSS) for remote sensing (GNSS-RS) purposes has been gaining in popularity in recent decades besides its primary services (timing, navigation, and positioning). Over 100 GNSS satellites, including GPS, Galileo, GLONASS, and BeiDou/Compass, transmit navigation signals. The signal generated by these satellites which pass through the atmosphere can contribute information about the atmospheric layers and their variability (Rajabi et al. 2020a, 2015). Reflected GNSS signals from land or oceans in a bi-static geometry provide an opportunity to study different parameters of the reflecting surfaces for natural hazards and environmental monitoring applications such as sea level (Martin-Neira 1993), sea surface roughness (Hoseini et al. 2020b), ocean eddies (Hoseini et al. 2020a), sea ice concentration (Semmling et al. 2019), flood (Rajabi et al. 2020b), precipitation (Asgarimehr et al. 2021), wind speed (Foti et al. 2017), snow depth (Tabibi 2016), river water height (Zeiger et al. 2021), and storm detection (Vu et al. 2019). This innovative technique represents a significant advancement in remote sensing, as it utilizes passive sensors that can operate effectively in ground-based, airborne, and space-borne modes (Zavorotny et al. 2014).

Ground-based GNSS-R as a multi-purpose sensor has been introduced as an alternative option for traditional tide gauges over the past decades. Compared to the tide gauges, this sensor is easier to install, covers a wider area, gives sea surface height in a global height coordinate system, is capable of correcting the station's vertical displacement, and can deliver extra information such as sea surface roughness and ice coverage. The conceptualization of sea level retrieval using GNSS-R was proposed in 1993 (Martin-Neira 1993) and used for ground-based GNSS-R stations signals in 2000 (Anderson 2000). Several studies have assessed the performance of the GNSS-R heights time series for tidal constituents analysis.

Semmling et al. (2012) used a 60-day GNSS-R height time series at Godhavn to detect diurnal (K_1) and semidiurnal (M_2, S_2) constituents with decimeter range. Löfgren et al. (2014) presented sea-level measurements retrieved from the analysis of signal-to-noise ratio (SNR) data recorded by five coastal geodetic GPS stations. They showed that the harmonic analysis of the residuals reveals remaining signal power at multiples of the GPS draconitic day. Furthermore, they illustrated that the observed SNR data were, to some level, disturbed by additional multi-path signals, in partic-

ular for GPS stations that are located in harbors. Larson et al. (2017) used 10 years of L1 SNR GPS data at Friday Harbor and found an RMSE of 12 cm from individual satellite passes. They showed that the tidal component (between S_a and M_6) retrieved from both the GNSS-R and tide gauge time series was in good agreement with the absolute differences of up to 1 cm in case of amplitudes. Tabibi et al. (2020) showed there is a millimetric agreement between SNR-based GNSS-R height and the tide gauge observation for eight major tidal components, except lunisolar diurnal (K_1), principal solar (S_2), and lunisolar semi-diurnal (K_2) components. They stated that differences were due to leakage from the GPS orbital period. Gravalon et al. (2022) used SNR-based GNSS-R at four stations and noticed an error in the $K1/K2$ tidal constituents. Geremia-Nievinski et al. (2020) utilized 1 year of SNR data for the GPS L1-C/A signal collected at the Onsala Space Observatory and compared the performance of the methods developed by four research groups. They concluded that all four groups captured semi-diurnal and diurnal variations and most GNSS-R solutions showed harmonics at integer fractions of one sidereal day.

In most of the GNSS-R studies, the tidal harmonics with periods shorter than 3 h (higher harmonics) are poorly represented due to the low temporal resolution of the measurements (Geremia-Nievinski et al. 2020). The studies predominantly utilized L1 SNR observations from geodetic receivers. This study uses around 6 years of In-phase and Quadrature (I/Q) datasets collected by multi-front-end dedicated GNSS-R receiver located in the Onsala Space Observatory. We evaluate the effect of using more observations at lower level, i.e., direct I/Q outputs, to retrieve SL variations. The final SL is the result of a combination of L1 and L2 generated height using a Left-Handed Circular Polarization (LHCP) antenna for detecting and analyzing the tidal harmonics. We estimate the SL using a 15-minute averaging window (near real-time and combined SL product) to increase time resolution. The rest of this paper is organized as follows. The study area and dataset are presented in Sect. 2. The methodology and mathematical concepts are described in Sect. 3. The discussion of data processing and the results are explained in Sect. 4. Finally, the paper is finalized by a conclusion in Sect. 5.

2 Data

2.1 GNSS-R site and dataset

We use just under 6 years of GNSS-R data from July 2015 to May 2021 obtained from a dedicated GNSS-R site mounted and operated by the German Research Center for Geosciences (GFZ) together with Onsala Space Observatory in Sweden (57.393° N, 11.914° E). The experiment uses multi-

ple antennas installed on a concrete structure with a height of about 3 m from the sea surface. The station has three types of antennas, one is zenith-looking and the two others are tilted toward the sea with the angle of 98° relative to the zenith. The zenith-looking antenna is RHCP and is assigned to track direct GPS signals. The sea-looking antennas with RHCP and LHCP can effectively acquire reflected GPS signals at two different polarizations with the highest antenna gain values of up to 4.7 dB. A GNSS occultation, reflectometry, and scatterometry (GORS) receiver (Rajabi et al. 2021a; Helm et al. 2007) with four antenna inputs is used in the GNSS-R site. The receiver can only process GPS L1 and L2 signals. The first input is utilized for the master channel and is linked to the up-looking antenna. The second and third inputs are dedicated to the slave channels and are connected to the sea-looking antennas.

Based on our previous study (Rajabi et al. 2022), the best performance for the altimetry can be achieved using the LHCP antenna. Therefore, we just use the data output of the LHCP link. To select valid observations which include reflected signals from the sea surface, the location of the specular points is calculated via a ray-tracing algorithm described by Semmling et al. (2016) concerning the earth's surface curvature. Afterward, we select the reflections from the sea surface using a polygon mask. The observations with elevation angles between 5° and 30° are selected for the investigation. The I/Q data with elevation angles below 5° are excluded to reduce the atmospheric effect and the rest of the effect is considered negligible because of the low reflector height. However, the atmospheric effect could introduce a small-scale error proportional to the reflector height (Williams and Nievinski 2017). As will be presented in the results section, the retrieved amplitudes from GNSS-R and the tide gauge show very close correspondence, highlighting a minimal atmospheric effect.

Figure 1a, b shows the GNSS-R experiment setup from the top view and the antenna installation setup. The data suffer from some gaps accounting for about 21% of the whole data. Although the method used in this study can handle datasets with gaps, the presence of missing values in the analyzed GNSS-R dataset can leave its signature on the accuracy of the results. In order to create the same situation for both datasets in the analysis, we utilize tide gauge measurements only at the epochs when GNSS-R data is available.

2.2 Tide gauge measurements

The dataset used in this study includes ancillary sea-level measurements from a nearby tide gauge located about 300 m away from our GNSS-R experiment setup (Fig. 1a). The tide gauge (Fig. 1c) was developed and constructed in-house, with advice from the Swedish Meteorological and Hydrological Institute (SMHI). The official tide gauge sta-
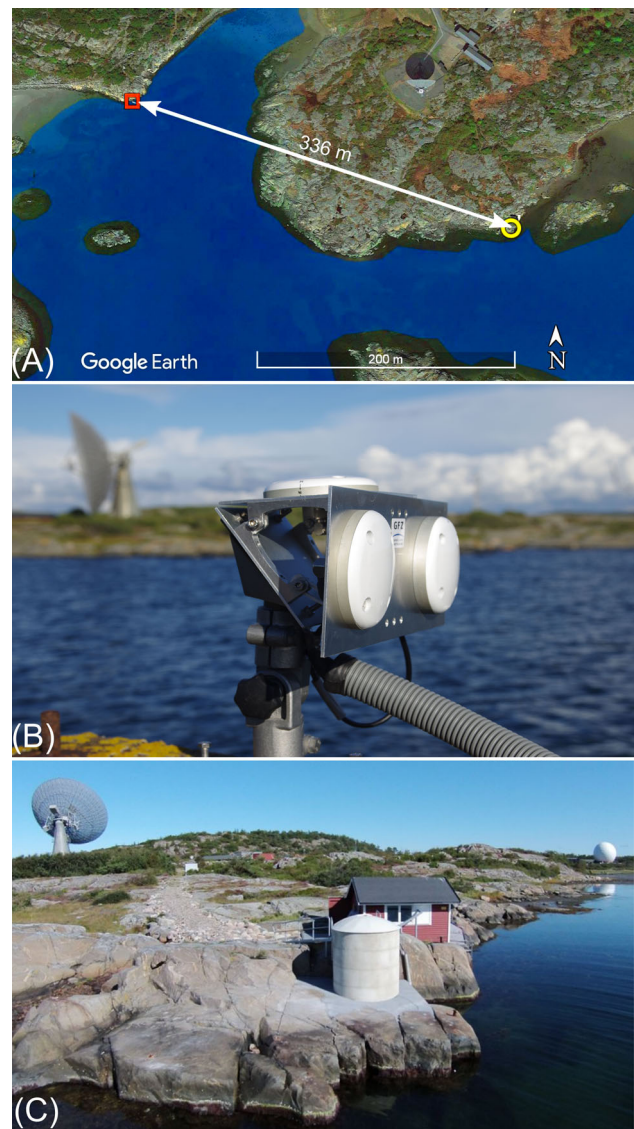

Fig. 1 **a** The red square and yellow circle represent the GNSS-R experiment setup and the tide gauge station from the top view, respectively, **b** the GNSS-R station antenna configuration, **c** the tide gauge station located in Onsala Space Observatory

tion consists of several sensors, and the main sensor is the Campbell $CS476$ radar with an 8° beam angle and millimeter-level accuracy. The data are open access through the SMHI website (https://www.smhi.se/kunskapsbanken/oceanografi/tide-gauge-onsala-1.94732).

3 Method

This study consists of three main stages (Fig. 2). The first stage is the data preparation through the time series associated with each reflection event. In the second stage, we focus on finding the interferometric frequency in the I/Q
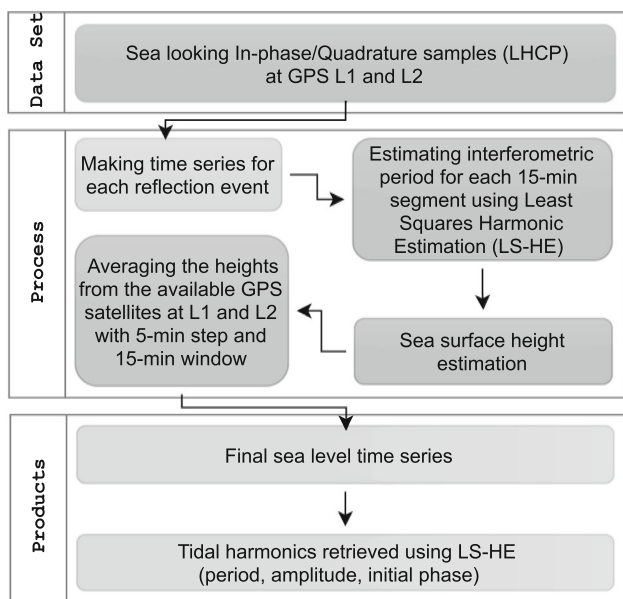
Fig. 2 A schematic diagram of methodology based on the univariate and multivariate least-squares harmonic estimation (LS-HE) method

observations using multivariate least-squares harmonic estimation (LS-HE) for the LHCP antenna. Then, we calculate the sea surface heights based on the retrieved interferometric frequency from L1 and L2 observations. To combine the estimated sea surface heights from different satellites, we use an averaging window of 15 min for every 5 min time step. Overall, each height measurement is based on up to eight reflection events from one to four satellites at L1 and L2 frequencies satellites reflection. We use a native MATLAB function for outlier detection based on the median absolute deviation (MAD) values. All the values beyond three scaled MAD with respect to the median are considered as outliers. To suppress the effect of any remaining outliers, the median value of the estimates within the averaging window is considered as the final height estimate. The last stage of the methodology is the validation of the GNSS-R height estimates with the collocated tide gauge observations and detecting the tidal harmonics for both datasets, and comparing them in terms of amplitudes, period, and initial phases.

3.1 GNSS-R height estimation

The interference of a reflected signal with the direct signal generates a compound signal. The SNR of the compound signal fluctuates due to the constructive or destructive phases of the direct and reflected signals. This oscillation is known as interference pattern and can be used to retrieve different information from the reflecting surface. Here, we aim to retrieve sea-level variations from the interference patterns. The geometry of reflection affects the frequency of the oscillation. Therefore, the main observation used in this study is

the interferometric frequency. We apply the LS-HE method to I/Q observations to effectively detect this frequency. The method uses individual linear terms for the I/Q time series. The linear terms can compensate the effect of the direct signal on the time series variations. Therefore, the LS-HE can separate the contributions of the direct signal from the interferometric fringes. The interferometric period are then inverted to the reflector height, i.e., the height between the phase center of the receiving antenna and the reflecting surface. The details of this procedure are given in (Rajabi et al. 2022).

The reflected signals travel an excess path to reach the antenna. The path difference between the direct and reflected signals ($\delta\rho$) changes over time which creates a Doppler frequency shift (δf) that characterizes the interferometric pattern's frequency (Hoseini et al. 2020b):

$$\delta f = \frac{1}{\lambda}\frac{d(\delta\rho)}{dt} \tag{1}$$

where λ is the carrier signal's wavelength. We use the period of interferometric oscillations to calculate the sea surface height. As shown in Fig. 3, $\delta\rho$ can be estimated by:

$$\delta\rho = 2\,h\,\sin(e) \tag{2}$$

with e being the satellite elevation angle, h the height difference between the sea surface and the antenna phase center. The variable $x = 2\sin(e)/\lambda$ is used here to simplify the calculations. The frequency of interferometric fringes in terms of the variable x is shown by δf_x and can be formulated as:

$$\begin{aligned}\delta\rho &= \lambda\,h\,x \\ \delta f_x &= \frac{1}{\lambda}\frac{\mathrm{d}(\delta\rho)}{\mathrm{d}x} = h + x\,\frac{\mathrm{d}h}{\mathrm{d}x} = h + x\,\dot h\,\frac{\mathrm{d}t}{\mathrm{d}x}\end{aligned} \tag{3}$$

where $\dot h = \mathrm{d}h/\mathrm{d}t$ is the rate of change for the reflector height. We apply an iterative process to simultaneously estimate the effect of height rate and retrieve accurate reflector height. In doing so, we first apply LS-HE method denoted by $\mathcal{L}$ to the I/Q samples of the LHCP slave antenna with respect to x:

$$\begin{aligned}P(T_x) &= \mathcal{L}(x, Y) \\ Y &= [I_s^L, \; Q_s^L] \\ \{P_{\max}, T_{\text{int}}\} &= \max[P(T_x)] \\ h &\approx \delta f_x = \frac{1}{T_{\text{int}}}\end{aligned} \tag{4}$$

where $P(T_x)$ is the output of LS-HE spectral analysis, which is a power spectrum against different periods, Y is the matrix of I/Q time series. The superscript L is used to refer to the LHCP polarization of the slave antenna denoted by the subscript s. The function max detects the maximum power and
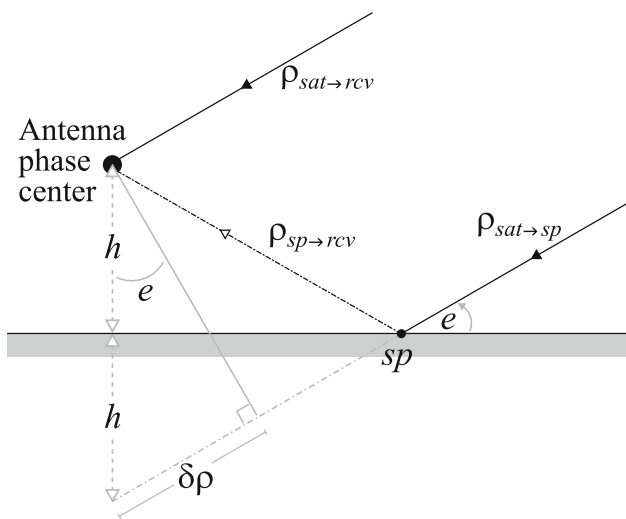
Fig. 3 The path difference between the direct and reflected signals in a ground-based reflectometry experiment with low reflector height. ρ_{sat-sp} is the distance between the satellite and specular point, $\rho_{sat-rec}$ is the distance between the satellite and receiver antenna, ρ_{sp-rec} is the distance between the specular point and receiver antenna, e is the satellite elevation angle, $\delta\rho$ is the extra path of the reflected signal compared to the direct signal, and h is the height difference between the phase center of the antenna and sea surface

returns the corresponding period, which is the period of interferometric pattern (T_{int}). The iterative process to find the accurate reflector height starts with the assumption $\dot{h} = 0$. The values of h and $\dot{h}$ are calculated within the following minimization problem (Rajabi et al. 2022):

$$\min_{h,\dot{h}} \sum_i^2 \left\| \hat{Y}_i - a_i \sin\left(\frac{4\pi[h + \delta h]\sin(e)}{\lambda} + \phi_i\right) \right\| \quad (5)$$

$$\delta h = \frac{\dot{h}\tan(e)}{\dot{e}} \quad (6)$$

where δh is the height rate correction, $\dot{e}$ denotes the rate of satellite elevation angle, $\hat{Y}_i$ are the detrended I/Q time series (linear trends removed), and a_i and ϕ_i are the amplitude and initial phase of the interferometric oscillation.

3.2 Least-squares harmonic estimation (LS-HE)

The LS-HE method is utilized in our study for retrieving sea-level variations from the GNSS-R I/Q interferometric observations and for the tidal harmonics analysis. The height retrieval uses multivariate LS-HE formulation while the tidal harmonics detection is based on univariate LS-HE. The multivariate LS-HE, as an extension of univariate harmonics estimation, can detect the common-mode signals in a set of multiple time series (Amiri-Simkooei et al. 2007). In the following, a brief introduction to this method is pro-

vided. Further details can be found in (Amiri-Simkooei 2013; Amiri-Simkooei et al. 2007; Rajabi et al. 2020a).

3.2.1 Univariate model

Observation equations can be modeled through the following linear model, which includes deterministic and stochastic parts of the time series (Amiri-Simkooei 2013):

$$E(y) = Ax, \quad D(y) = Q_y, \quad (7)$$

with $E(\bullet)$ and $D(\bullet)$ indicating the expectation and dispersion operators. Deterministic behavior of the time series is captured by the first term $E(y) = Ax$ and the second term provides a stochastic model to describe the statistical characteristics of the observations. The vector of unknowns includes elements describing a low-order polynomial, e.g., two unknowns for a linear regression model.

Under null hypothesis, we assume that Eq. (7) can adequately model the time series. The model can be improved under the alternative hypothesis. For any periodic signal in the time series, the deterministic part of the model can be extended by a two-column design matrix A_k:

$$E(y) = Ax + A_k x_k, \quad D(y) = Q_y, \quad (8)$$

where the unknown vector x_k contains two elements to estimate the amplitudes of the signal $a_k \cos(\omega_k t) + b_k \sin(\omega_k t)$ at a frequency of ω_k. The unknown frequencies ω_k are detected through LS-HE, i.e., by maximizing the following functional:

$$\omega_k = arg \max_{\omega_j} P(\omega_j), \quad (9)$$

where

$$P(\omega_j) = \text{tr}(\hat{e}^T Q_y^{-1} A_j (A_j^T Q_y^{-1} P_A^\perp)^{-1} A_j^T Q_y^{-1} \hat{e}), \quad (10)$$

where tr is the trace operator and the least-squares residuals are $\hat{e} = P_A^\perp y$ with $P_A^\perp = I - A(A^T Q^{-1} A)^{-1} A^T Q^{-1}$ being an orthogonal projector. The values of $P(\omega_j)$ construct the power spectrum against a range of different frequencies. The frequency corresponding to the maximum value of the power spectrum indicates the frequency of interest, i.e., ω_K. The statistical significance of the detected frequency can be verified through a hypothesis testing procedure using the test statistic $T_k = P(\omega_j) = tr(\hat{e}^T Q_y^{-1} A_k (A_k^T Q_y^{-1} P_A^\perp)^{-1} A_k^T Q_y^{-1} \hat{e})$. Under the null hypothesis, if the covariance matrix Q_y is known and the distribution of the time series is normal, the test statistic has a central Chi-square distribution with 2 degrees of freedom. The detected frequency is statistically significant if the null hypothesis is rejected. The detection process can be repeated for other frequencies with the new design matrix $A = [A \; A_k]$.

3.2.2 Multivariate model

The LS-HE can be utilized for detecting common periodic signals in multiple time series through a multivariate power spectrum. Each time series can have a dedicated polynomial model with its corresponding unknown coefficients. In this case, if the design matrix A and covariance matrix Q_y are the same for all the time series, the deterministic model can be referred to as multivariate model represented by (Amiri-Simkooei 2013):

$$E(\text{vec}(Y)) = (I_r \otimes A) \, \text{vec}(X) + (I_r \otimes A_k)\text{vec}(X_k) \quad (11)$$

with the multivariate covariance matrix

$$D(\text{vec}(Y)) = \Sigma \otimes Q, \quad (12)$$

with r being the number of the time series, $\otimes$ the Kronecker product, I the identity matrix, and vec the vector operator. A and A_k are the design matrices.

The second term in Eq. (11) includes the element $(I_r \otimes A_k)$ which is meant to capture a common periodic pattern across all the time series. The common periodicity can have different phase and amplitude in different time series. The matrix Y is the observations matrix, which includes the time series as its columns. The matrices X and X_k are the unknowns. The frequency (ω_k) can be detected through the maximization of Eq. (9) with:

$$P(\omega_j) = \text{tr}(\hat{E}^T Q^{-1} A_j (A_j^T Q^{-1} P_A^\perp)^{-1} A_j^T Q^{-1} \hat{E} \hat{\Sigma}^{-1}), \quad (13)$$

where $P(\omega_j)$ denotes the multivariate power spectrum, $\hat{E} = P_A^\perp Y$ is the least-squares residuals matrix and $P_A^\perp = I - A(A^T Q^{-1} A)^{-1} A^T Q^{-1}$ is the orthogonal projector and $\hat{\Sigma} = \hat{E}^T Q^{-1} \hat{E}/(m-n)$. The following test statistic can be used for testing the significance of the detected signal:

$$T = P(\omega_k) = \text{tr}(\hat{E}^T Q^{-1} A_k (A_k^T Q^{-1} P_A^\perp)^{-1} A_k^T) \quad (14)$$

If Σ and Q are known and the original observations follow a normal distribution, the test statistic T under the null hypothesis is considered to follow a central Chi-square distribution with $2r$ degrees of freedom, i.e., $T \sim \chi^2(2r, 0)$ with r being the number of the time series (Amiri-Simkooei 2013).

3.3 Applications of the LS-HE to height retrieval and tidal harmonics detection

We first apply multivariate LS-HE for SL calculation. The multivariate formulation provides a robust tool to find common-mode interferometric period in the I/Q time series

obtained from the GNSS-R receiver. The SL time series from GNSS-R and the nearby tide gauge are then analyzed by the univariate LS-HE to characterize the tidal harmonics.

The LS-HE method performs a numerical search to catch the dominant harmonic signals in the time series. The step size for finding the harmonic signals is determined with the following recursive formula:

$$T_i = T_{i-1} \left(1 + \alpha \, \frac{T_{i-1}}{T_{\max}} \right), \quad \alpha = 0.01, \quad i = 1, 2, \ldots, T_i \le T_{\max}, \quad (15)$$

with T_i being the trial periods, T_0 and $T_{\max}$ the minimum and maximum periods in the time series based on Nyquist's theorem, respectively. The coefficient α controls the resolution or step of searching the periods. The recursive formula creates smaller step size for shorter periods and larger step size for longer periods. We assume the covariance matrix is the Identity matrix $Q_y = I$ for each time series. The observation matrices used in the SL retrieval and in the tidal harmonics analysis are as follows:

Observations matrix for finding interference pattern:

$$Y = [I, \ Q]$$

Observations matrix for tidal harmonic:

$$Y = [h_{\text{GNSS}}], \ Y = [h_{\text{TG}}] \quad (16)$$

It should be noted that univariate formulation of LS-HE with $Q_y = I$ will act similar to the ordinary least-squares method.

3.4 Phase and amplitude estimation

We use the U-tide MATLAB package (Codiga 2011), implemented according to the equilibrium tide theory (Foreman and Henry 1989) for deriving the amplitude and phase of a standard table of tidal constituents from the GNSS-R and tide gauge SL measurements. The following model is used for the estimation of the amplitude and phase of the tidal constituents [equation (6) in Foreman et al. (2009)]:

$$h(t_j) = Z_0 + a \, t_j + \sum_{k=1}^{n} f_k(t_j)[X_k \, \cos\,(V_k(t_j) + u_k(t_j))$$
$$+ \, Y_k \, \sin\,(V_k(t_j) + u_k(t_j))] + R(t_j) \quad (17)$$

where X_k and Y_k are:

$$X_k = A_k \, \cos\, g_k, \quad (18)$$
$$Y_k = A_k \, \sin\, g_k \quad (19)$$

with $h(t_j)$ being the SL measurement at the time t_j; Z_0 and a are the unknown linear terms, and for each constituent k

Fig. 4 Examples of observation time series of PRN 26 for one segment which are used to retrieve interferometric period (T_{int}) using multivariate LS-HE formulation. **a** The In-phase and Quadrature components for GPS L1 and L2 for the LHCP antenna. **b** The dominant interferometric period retrieved by applying LS-HE method to the combinations of the I/Q time series
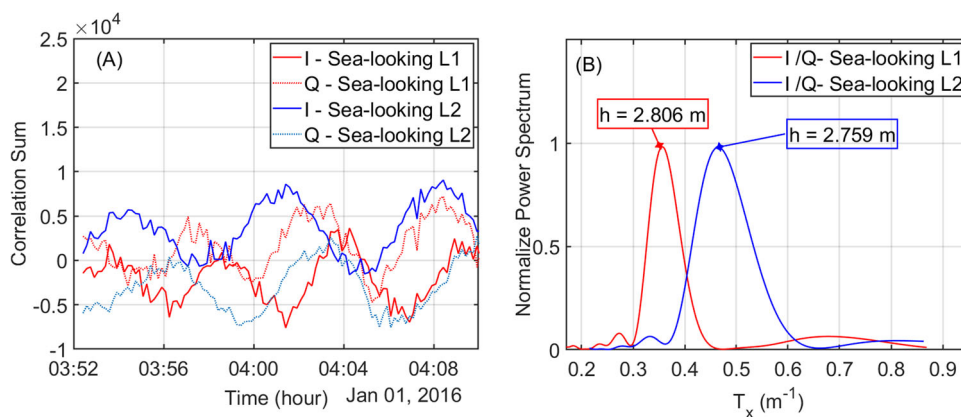
the unknown amplitude and phase are, respectively, denoted by A_k and g_k. In the process of tidal harmonic analysis, the unknown parameters are estimated by minimization of the residuals $R(t_j)$, while the nodal corrections (Godin 1972) to the amplitude ($f_k(t_j)$) and phase ($u_k(t_j)$), and the astronomical argument $V_k(t_j)$ (Godin 1972) can be calculated for each constituent k at the time of sea-level measurement t_j (Foreman et al. 2009).

4 Results and discussion

The performance of SL retrieval from the I/Q interference patterns at different antenna settings and sea states has been already discussed in (Rajabi et al. 2021a, b, 2022). According to these investigations, the sea-looking LHCP antenna performs better compared to both up- and sea-looking RHCP antennas. The improvement is significant and can reach 48% and 50% for L1 and L2 frequencies, respectively. Moreover, combining the SL measurements from L1 and L2 improves the accuracy of final sea surface heights by up to 25% and 40%. Therefore, we use the SL measurements from the combined L1 and L2 I/Q observations of the sea-looking LHCP antenna. The measurements have a temporal resolution of 5 min. This setting is chosen to provide an adequate dataset for retrieving tidal harmonics.

In the first step, we down-sampled I/Q correlation sums to a 10-second (0.1 Hz) integration due to the outputs of the GORS receiver being based on 5-millisecond coherent integration time (200 Hz sampling rate). Afterward, we prepared the 15 min time series of I/Q with the time step of 1 min for extracting interferometric pattern periods using multivariate LS-HE to calculate L12 SL with an averaging window of 15 min and 5-minute time step. The multivariate analysis improves the detection by utilizing common-mode signals from the different GNSS-R time series by amplifying the power of the retrieved signals. Figure 4 visualized an example estimation of the LS-HE on the time series which is generated from a 15 min segment for satellite PRN 26 in L1 and
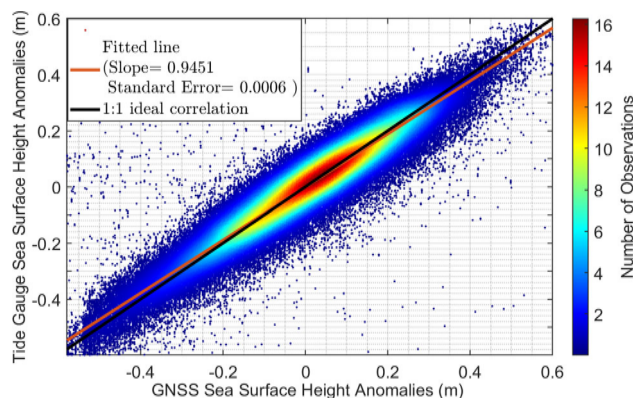
Fig. 5 Scatter plot of the GNSS-R and tide gauge height anomalies with the time step and averaging window of 5 and 15 min, respectively. The fitted line and 1:1 ideal correlation are shown by the solid red line and black line, respectively

L2 signals. Figure 4a shows the I and Q components from the LHCP antenna in different frequencies, and Fig. 4b depicts the harmonic analysis results for L1 and L2, including estimated heights.

Figure 5 compares the sea surface height variations from GNSS-R and tide gauge measurements. The SL variations from the two datasets show a high level of agreement. The red is the fitted line to the corresponding measurements from the datasets, and the black line illustrates the ideal 1:1 line. The RMSE between GNSS-R L12 sea surface heights with collocated tide gauge observations is 5.8 cm with a correlation of 0.948.

We utilize the univariate LS-HE method for detecting the tidal harmonics in the GNSS-R L12 and tide gauge sea-level time series. Figure 6a illustrates the tidal periods retrieved from both GNSS-R estimated and tide gauge heights. These plots show the detected periodic harmonics until the annual and semiannual tidal harmonics S_a and S_{sa}. S_a and S_{sa} are smaller than other tidal constituents and insignificant for most applications, but their estimated values are much larger than would be reasonable from astronomical forcing due to

Fig. 6 The least-squares power spectrum of the tidal harmonics detected in the GNSS-R and tide gauge (TG) sea-level measurements. The measurements cover a period of 6 years with a temporal resolution of 5 min. **a** The overall Periodogram produced by applying the univariate LS-HE to the GNSS-R and tide gauge data. **b** The power ratio between the two periodograms. **c, d** Provide zoomed views of the detected tidal harmonics with periods between 3 to 30 and 0.5 to 3 h, respectively
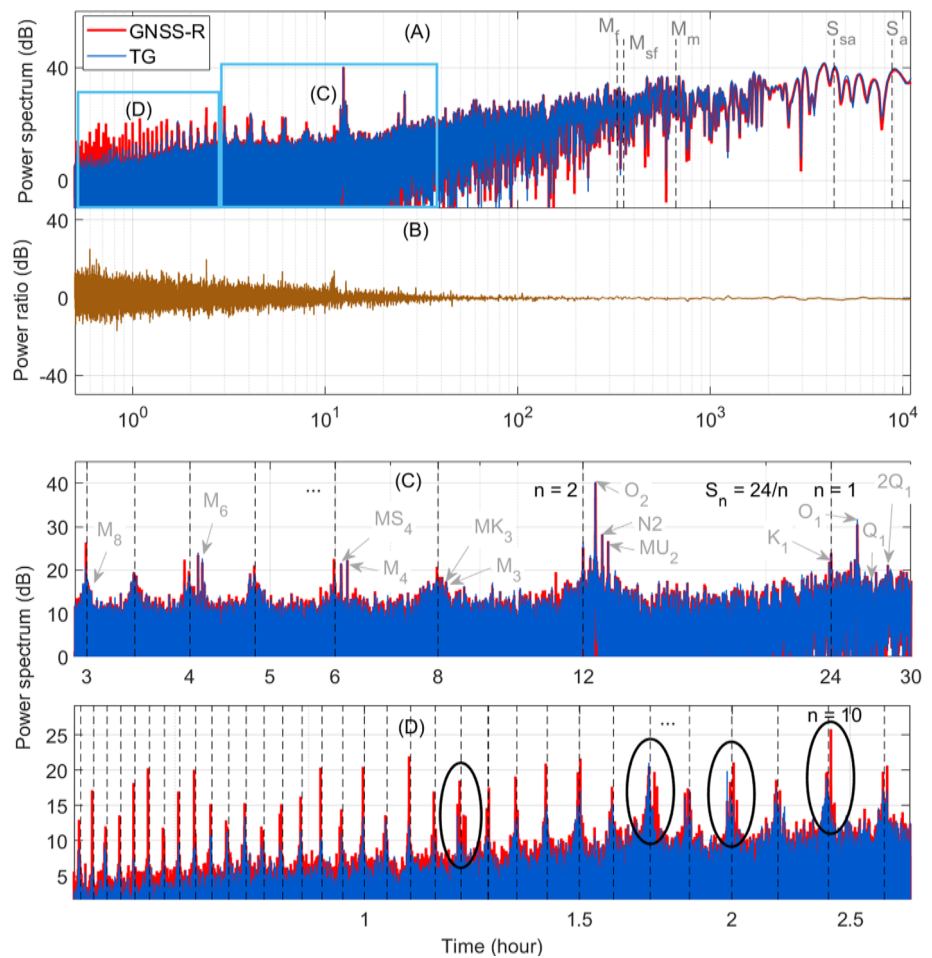
the seasonal changes in wind, temperature, and atmospheric pressure. Overall, the detected harmonics from the GNSS-R and tide gauge time series coincide very well. For instance, both sensors could successfully capture the periodicity of the lunar monthly constituent (M_m), lunar synodic fortnightly constituent (M_{sf}), and lunar fortnightly constituent (M_f). Figure 6b depicts the ratio of the GNSS-R and tide gauge power spectra. The variation of the power ratio is mostly distributed equally around zero.

Two parts of the spectra shown in Fig. 6a are magnified and presented in Fig. 6c, d. Figure 6c depicts the detected harmonics with periods between ≈ 3 and 30 h and Fig. 6d covers the periods ranging from 30 min to just below 3 h. The periodograms in Fig. 6c, d show the main tidal harmonic constituents segment the period spectrum with the central harmonics of $S_n = 24/n, n = 1, 2, \ldots$. Several harmonics are detected around the S_n harmonics. The results which the tidal harmonics are around S_n in the spectral analysis agree with the tidal analysis presented by Amiri-Simkooei et al. (2014). For better visualization, some of the harmonics by Darwin's symbols are marked in Fig. 6a, c. Both of the datasets can similarly capture the main tidal frequencies, e.g.,

the tidal periods longer than one day (bi-monthly, monthly, semiannual), the solar diurnal signal, and its higher harmonics (S_n), lunar diurnal and higher harmonics ($O_1, K_1, \rho_1, M_2, N_2, M_3, M_4$ and M_6), lunisolar diurnal (K_1) and variational (MU_2) and shallow waters (i.e., MK_3).

Figure 6d shows the detected tidal harmonics with periods below 3 h. The periodograms shown in Fig. 6 confirm the overall excellent performance of the GNSS-R measurements. However, we have detected some harmonics in GNSS-R time series (marked by a green ellipsoid in Fig. 6d) that are not well-accompanied by TG counterparts. In this area, some GNSS-R retrieved picks are stronger than TG and are closer to the standard tidal periods. For example, standard tenth-diurnal tidal constituents (according to the standard tidal constituents list of the tide, water level and current working group of international hydrographic organization (https://iho.int/en/twcwg) start from 2.431 to 2.511 h, and the estimated period by GNSS data is around 2.428 compared to 2.390 from TG. For the case of fourteenth-diurnal with the period of 1.766 to 1.770 h in the standard tide table, GNSS-R detects sharp peaks from 1.728 to 1.741 in contrast to a less prominent TG peak at 1.724 h. Therefore, GNSS-

Table 1 The amplitudes and initial phases of the standard tidal constituents up to the annual period which were detected by the univariate least-squares harmonic estimation of 6-year time series for both tide gauge (TG) and GNSS-R

Darwin's symbol	Period (h)	Amp_T (cm)	Amp_G (cm)	Δ_{Amp}	ϕ_T°	ϕ_G°	$\text{abs}(\Delta_{phi}^\circ)$
Long periods							
S_a	8766.2315	4.57	4.40	0.18	290.9	287.5	3.4
S_{sa}	4382.9063	5.46	5.17	0.29	256.4	254.7	1.7
M_m	661.3092	2.27	2.13	0.14	170.2	172.2	2.0
M_{sf}	354.3671	0.87	0.83	0.05	145.6	142.4	3.2
M_f	327.8590	1.11	0.94	0.17	208.7	211.3	2.6
Diurnals							
$2Q_1$	28.0062	0.34	0.33	0.02	260.4	263.1	2.7
Q_1	26.8684	0.43	0.38	0.05	257.9	266.5	8.6
ρ_1	26.7231	0.27	0.25	0.02	277.6	289.1	11.6
O_1	25.8193	2.25	2.04	0.21	299.0	301.9	3.0
M_1	24.8332	0.33	0.34	0.00	335.3	326.4	8.9
P_1	24.0659	0.29	0.30	0.00	278.0	305.4	27.5
S_1	24.0000	0.94	1.03	-0.09	27.6	40.0	12.4
K_1	23.9345	0.47	0.09	0.37	308.8	52.8	104.0
J_1	23.0985	0.12	0.11	0.00	156.2	170.8	14.6
OO_1	22.3061	0.10	0.13	-0.03	288.6	238.3	50.2
Semi-Diurnals							
$2''N_2$	12.9054	0.15	0.12	0.03	38.3	59.4	21.1
MU_2	12.8718	1.08	1.13	-0.06	316.2	319.1	2.9
N_2	12.6583	1.30	1.31	-0.01	108.7	112.5	3.9
V_2	12.6260	0.47	0.50	-0.02	135.7	131.5	4.2
M_2	12.4206	5.32	5.28	0.04	151.4	153.4	2.0
λ_2	12.2218	0.35	0.32	0.04	260.0	265.4	5.4
L_2	12.1916	0.60	0.63	-0.04	277.3	282.1	4.8
T_2	12.0164	0.17	0.09	0.07	122.4	85.4	37.0
S_2	12.0000	1.13	1.00	0.13	106.1	101.2	4.9
R_2	11.9836	0.13	0.19	-0.06	315.6	308.2	7.5
K_2	11.9672	0.21	0.20	0.01	70.2	338.8	91.4
Higher harmonics							
$2''MK_3$	8.3863	0.22	0.22	0.00	8.1	352.1	16.0
M_3	8.2804	0.15	0.14	0.01	26.0	18.6	7.4
MK_3	8.1771	0.16	0.16	0.00	254.3	348.9	94.6
MN_4	6.2692	0.21	0.19	0.02	296.5	304.7	8.2
M_4	6.2103	0.73	0.70	0.03	302.9	309.1	6.2
MS_4	6.1033	0.49	0.50	-0.01	31.7	39.3	7.6
S_4	6.0000	0.14	0.13	0.01	27.8	4.5	23.3
M_6	4.1402	0.72	0.63	0.09	65.4	69.7	4.3
M_8	3.1052	0.05	0.04	0.01	337.7	355.0	17.2

Amp_T (cm) and Amp_G (cm) denote the amplitudes related to TG and GNSS-R, respectively. ϕ_T° and ϕ_G° are the initial phases of the TG and GNSS-R, respectively. $\Delta_{\text{Amp}} = \text{Amp}_G - \text{Amp}_T$ is the differences between the GNSS-R and TG amplitudes

Fig. 7 The estimated amplitudes of standard tidal constituents retrieved from GNSS-R and Tide Gauge observations. The blue bars are related to the GNSS-R, and the red bars show the tide gauge estimates. The circles above the bars visualize the relative error between GNSS-R and tide gauge amplitudes by their sizes and colors. Horizontal axes are labeled by the Darwin Symbol clarified in Table 1
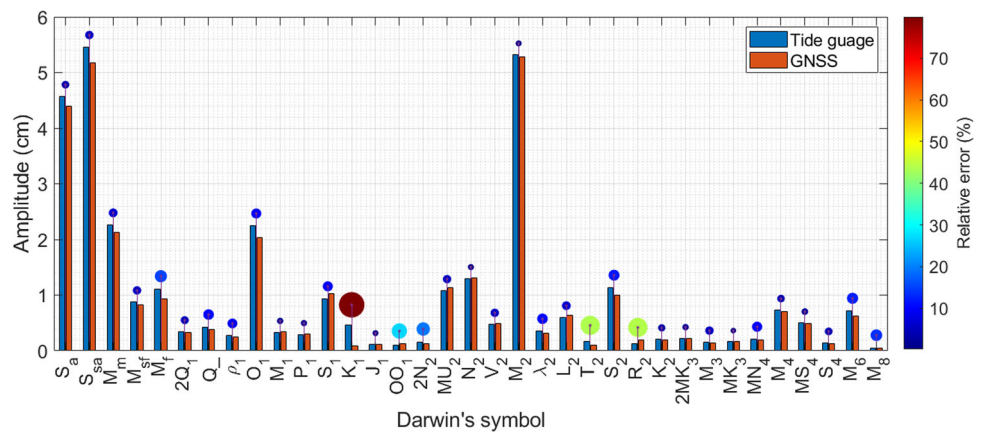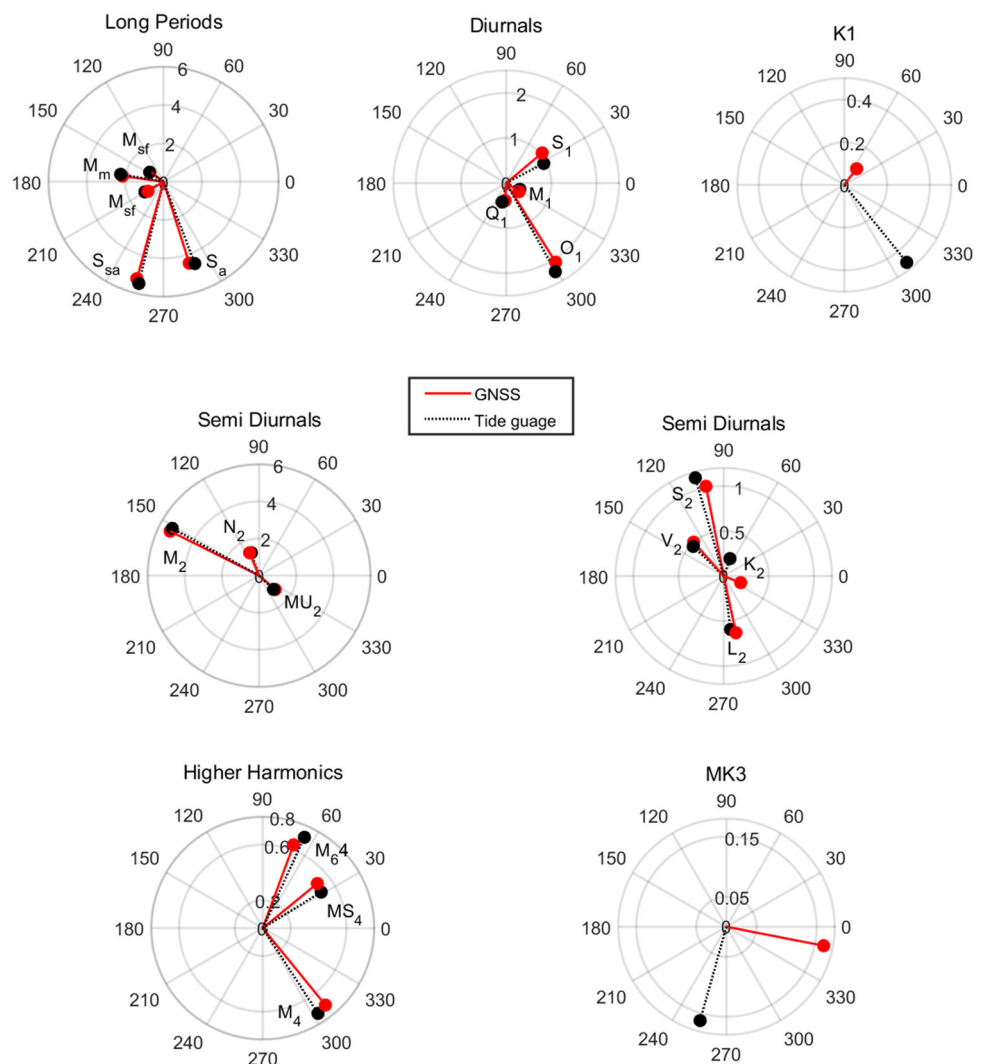

Fig. 8 Comparison of amplitudes and phases of the most important tidal harmonics at Onsala stations based on polar representation. The amplitudes are shown in centimeter and the phases are in degrees

shows a better performance in detecting higher harmonics. Geremia-Nievinski et al. (2020) investigated the capability of GNSS-R using the least-square method in Onsala to capture tidal harmonics between 3 and 30 h. Their results confirm that GNSS-R is successful in capturing the dominant tidal constituents. However, long periods of tidal harmonics are less discussed in the GNSS-R studies due to the limited time span of the datasets. The same issue applies to the period shorter than 3 h because of the temporal resolution of the retrieved sea levels. For example, Semmling et al. (2012) could detect the diurnal ($K1$) and semi-diurnal harmonics ($M2$, $S2$) in Godhavn. Löfgren et al. (2014) report their tidal analysis and the captured periods (semi-diurnal up to semiannual) in five different stations, one of which is located in Onsala. This study investigates tidal harmonics with a wide range of periods from 30 min to 1 year using a relatively long dataset. It should be noted that the GNSS-R station used in the two studies mentioned above in Onsala are different from our experiment and are based on SNR observations from geodetic receivers.

Table 1 lists the amplitudes larger than the 1-sigma confidence interval and the initial phases of the standard tidal constituents estimated from the tide gauge and GNSS-R. The table highlights an overall good agreement between the tide gauge and GNSS-R results, suggesting that the GNSS-R sea-level products can effectively be used for the tidal analysis purposes. As can be seen from Table 1, the most significant difference of 3.7 mm between the amplitudes belongs to K_1 constituent as depicted in Fig. 7. The figure visualizes Table 1 regarding amplitude and relative errors between two datasets. The blue and red bars show the amplitudes of the tidal harmonics retrieved from GNSS-R and TG observations, respectively. The size and color of the circles above the bars illustrate the relative error between the estimated amplitudes in percentage. The relative errors are calculated as the difference of the two amplitudes divided by the tide gauge amplitude. Figure 8 highlights the agreements and discrepancies between the estimated phase values of GNSS-R and tide gauge using the polar coordinate system. The estimated phase values from GNSS-R measurements for harmonics K_1, $O O_1$, K_2, and $M K_3$ show large deviations from the tide gauge estimates, although they have relatively small amplitudes at the site. The GPS orbital period can be one the main contributors to the observed differences as reported by previous studies (e.g., Tabibi et al. (2020), Larson et al. (2017), Löfgren et al. (2014)). This effect is more noticeable in phase of the tidal harmonics.

Our estimated amplitudes for daily and sub-daily harmonics agree with a similar study at Onsala by Löfgren et al. (2014). However, for the monthly and semiannual harmonics the differences are significant. These differences can stem from the fact that the results presented here are based on measurements at higher temporal resolution from I/Q observations over much longer time span (6 years compared to six months).

5 Conclusion

This study investigated the potential of ground-based GNSS-R technique for detecting and analyzing tidal constituents. The analysis is conducted using a relatively long dataset of 6 years obtained from a coastal GNSS-R experiment installed at Onsala Space Observatory. A highlight of this study was to utilize dual-frequency I/Q interferometric observations to retrieve sea level and tidal harmonics. We applied uni- and multivariate least-squares harmonic estimation (LS-HE) method for sea-level calculation and estimating tidal constituents. The U-tide software is used to retrieve the amplitude and phase of a list of standard tidal harmonics. The RMSE value between GNSS-R sea surface heights for LHCP sea-looking antenna and collocated tide gauge measurements was 5.8 cm, with a correlation of 0.948. Our tidal harmonics analysis, owing to the long dataset and a high temporal resolution measurements of 5 min, could capture a broad range of periods, i.e., from 30 min to annual. Both the GNSS-R and tide gauge sea-level measurements showed similar performance in capturing tidal constitutes. However, the GNSS-R shows supremacy in detecting harmonics with the periods shorter than 3 h. Comparison of the estimated amplitude and phase of the standard tidal periods indicates a high level of agreement between the GNSS-R and tide gauge observations. However, a significant difference is observed for the amplitude and phase of the k_1 constituent. Moreover, the phase values of $O O_1$, K_2, and $M K_3$ constituents derived from GNSS-R are notably different compared to the tide gauge. As already reported in the literature, the orbital period of GPS is considered as one of the main affecting factors for the observed differences. It should be noted that these four constituents have very small amplitudes of less than 5 mm at Onsala. The study suggests that a dedicated GNSS-R setup based on the dual-frequency I/Q observations from sea-looking antenna, provides accurate tidal products.

Author Contributions MR and MH were involved in conceptualization; MRam, MA, and JW helped in GNSS-R experiment and data; MR and MH contributed to data curation; MR and MH were involved in formal analysis; MR, MG, and HN helped in funding acquisition; MR and MH contributed to investigation, methodology, visualization; MR, MH, and MS contributed to software; HN and JW helped in supervision; MR and

References

Adebisi N, Balogun AL, Min TH, Tella A (2021) Advances in estimating sea level rise: a review of tide gauge, satellite altimetry and spatial data science approaches. Ocean Coast Manag 208(105):632

Amiri-Simkooei AR, Tiberius CC, Teunissen PJ (2007) Assessment of noise in GPS coordinate time series: methodology and results. J Geophys Res Solid Earth 112(B7)

Amiri-Simkooei A (2013) On the nature of GPS draconitic year periodic pattern in multivariate position time series. J Geophys Res Solid Earth 118(5):2500–2511

Amiri-Simkooei A, Zaminpardaz S, Sharifi M (2014) Extracting tidal frequencies using multivariate harmonic analysis of sea level height time series. J Geod 88(10):975–988

Anderson KD (2000) Determination of water level and tides using interferometric observations of GPS signals. J Atmos Ocean Technol 17(8):1118–1127

Asgarimehr M, Hoseini M, Semmling M, Ramatschi M, Camps A, Nahavandchi H, Haas R, Wickert J (2021) Remote sensing of precipitation using reflected GNSS signals: response analysis of polarimetric observations. IEEE Trans Geosci Remote Sens. https://doi.org/10.1109/TGRS.2021.3062492

Church JA, White NJ (2011) Sea-level rise from the late 19th to the early 21st century. Surv Geophys 32(4):585–602

Cipollini P, Calafat FM, Jevrejeva S, Melet A, Prandi P (2017) Monitoring sea level in the coastal zone with satellite altimetry and tide gauges. In: Integrative study of the mean sea level and its components, pp 35–59

Codiga DL (2011) Unified tidal analysis and prediction using the UTide Matlab functions. Technical report 2011-01. Graduate School of Oceanography, University of Rhode Island, Narragansett

Devlin AT (2016) On the variability of pacific ocean tides at seasonal to decadal time scales: observed vs modelled. Ph.D. thesis, Portland State University

Doodson A (1954) Appendix to circular-letter 4-h. The harmonic development of the tide-generating potential. Int Hydrogr Rev 31:37–61

Foreman MGG, Henry RF (1989) The harmonic analysis of tidal model time series. Adv Water Resour 12(3):109–120

Foreman MG, Cherniawsky JY, Ballantyne V (2009) Versatile harmonic tidal analysis: improvements and applications. J Atmos Ocean Technol 26(4):806–817

Foti G, Gommenginger C, Srokosz M (2017) First spaceborne GNSS-reflectometry observations of hurricanes from the UK TechDemoSat-1 mission. Geophys Res Lett 44(24):12–358

Geremia-Nievinski F, Hobiger T, Haas R, Liu W, Strandberg J, Tabibi S, Vey S, Wickert J, Williams S (2020) SNR-based GNSS reflectometry for coastal sea-level altimetry: results from the first IAG inter-comparison campaign. J Geodesy 94(8):1–15

Godin G (1972) University of Toronto Press

Gravalon T, Seoane L, Ramillien G, Darrozes J, Roblou L (2022) Determination of weather-induced short-term sea level variations by GNSS reflectometry. Remote Sens Environ 279(113):090

Helm A, Montenbruck O, Ashjaee J, Yudanov S, Beyerle G, Stosius R, Rothacher M (2007) GORS-A GNSS occultation, reflectometry and scatterometry space receiver. In: Proceedings of the 20th international technical meeting of the Satellite Division of The Institute of Navigation (ION GNSS 2007), pp 2011–2021

Hoseini M, Asgarimehr M, Zavorotny V, Nahavandchi H, Ruf C, Wickert J (2020) First evidence of mesoscale ocean eddies signature in GNSS reflectometry measurements. Remote Sens 12(3):542

Hoseini M, Semmling M, Nahavandchi H, Rennspiess E, Ramatschi M, Haas R, Strandberg J, Wickert J (2020b) On the response of polarimetric GNSS-reflectometry to sea surface roughness. IEEE Trans Geosci Remote Sens

Larson KM, Ray RD, Williams SD (2017) A 10-year comparison of water levels measured with a geodetic GPS receiver versus a conventional tide gauge. J Atmos Ocean Technol 34(2):295–307

Löfgren JS, Haas R, Scherneck HG (2014) Sea level time series and ocean tide analysis from multipath signals at five GPS sites in different parts of the world. J Geodyn 80:66–80

Marti F, Cazenave A, Birol F, Passaro M, Léger F, Niño F, Almar R, Benveniste J, Legeais JF (2019) Altimetry-based sea level trends along the coasts of Western Africa. Adv Space Res

Martin-Neira (1993) A passive reflectometry and interferometry system (PARIS): application to ocean altimetry. ESA J 17(4):331–355

Rajabi M, Amiri-Simkooei A, Asgari J, Nafisi V, Kiaei S (2015) Analysis of TEC time series obtained from global ionospheric maps. J Geomat Sci Technol 4(3):213–224

Rajabi M, Amiri-Simkooei A, Nahavandchi H, Nafisi V (2020) Modeling and prediction of regular ionospheric variations and deterministic anomalies. Remote Sens 12(6):936

Rajabi M, Nahavandchi H, Hoseini M (2020) Evaluation of CYGNSS observations for flood detection and mapping during Sistan and Baluchestan Torrential Rain in 2020. Water 12(7):2047

Rajabi M, Hoseini M, Nahavandchi H, Semmling M, Ramatschi M, Goli M, Haas R, Wickert J (2022) Polarimetric GNSS-R sea level monitoring using I/Q interference patterns at different antenna configurations and carrier frequencies. IEEE Trans Geosci Remote Sens 60:1–13. https://doi.org/10.1109/TGRS.2021.3123146

Rajabi M, Hoseini M, Nahavandchi H, Semmling M, Ramatschi M, Goli M, Haas R, Wickert J (2021a) Performance assessment of GNSS-R polarimetric observations for sea level monitoring. In: EGU general assembly conference abstracts, pp EGU21–12709

Rajabi M, Hoseini M, Nahavandchi H, Semmling M, Ramatschi M, Goli M, Haas R, Wickert J (2021b) A performance assessment of polarimetric GNSS-R sea level monitoring in the presence of sea surface roughness. In: 2021 IEEE international geoscience and remote sensing symposium IGARSS, IEEE, pp 8328–8331

Rourke FO, Boyle F, Reynolds A (2010) Tidal energy update 2009. Appl Energy 87(2):398–409

Semmling A, Schmidt T, Wickert J, Schön S, Fabra F, Cardellach E, Rius A (2012) On the retrieval of the specular reflection in GNSS carrier observations for ocean altimetry. Radio Sci 47(06):1–13

Semmling AM, Leister V, Saynisch J, Zus F, Heise S, Wickert J (2016) A phase-altimetric simulator: Studying the sensitivity of Earth-reflected GNSS signals to ocean topography. IEEE Trans Geosci Remote Sens 54(11):6791–6802

Semmling AM, Rösel A, Divine DV, Gerland S, Stienne G, Reboul S, Ludwig M, Wickert J, Schuh H (2019) Sea-ice concentration derived from GNSS reflection measurements in Fram Strait. IEEE Trans Geosci Remote Sens 57(12):10,350-10,361

Shum C, Yu N, Morris CS (2001) Recent advances in ocean tidal science. J Geod Soc 47(1):528–537

Tabibi S (2016) Snow depth and soil moisture retrieval using SNR-based GPS and GLONASS multipath reflectometry. Ph.D. thesis, University of Luxembourg, Luxembourg

Tabibi S, Geremia-Nievinski F, Francis O, van Dam T (2020) Tidal analysis of GNSS reflectometry applied for coastal sea level sensing in Antarctica and Greenland. Remote Sens Environ 248(111):959. https://doi.org/10.1016/j.rse.2020.111959

Vu PL, Ha MC, Frappart F, Darrozes J, Ramillien G, Dufrechou G, Gegout P, Morichon D, Bonneton P (2019) Identifying 2010 Xynthia storm signature in GNSS-R-based tide records. Remote Sens 11(7):10. https://doi.org/10.3390/rs11070782

Williams S, Nievinski F (2017) Tropospheric delays in ground-based GNSS multipath reflectometry—experimental evidence from coastal sites. J Geophys Res Solid Earth 122(3):2310–2327

Zavorotny VU, Gleason S, Cardellach E, Camps A (2014) Tutorial on remote sensing using GNSS bistatic radar of opportunity. IEEE Geosci Remote Sens Mag 2(4):8–45. https://doi.org/10.1109/MGRS.2014.2374220

Zeiger P, Frappart F, Darrozes J, Roussel N, Bonneton P, Bonneton N, Detandt G (2021) SNR-based water height retrieval in rivers: application to high amplitude asymmetric tides in the Garonne River. Remote Sens 13(9):25. https://doi.org/10.3390/rs13091856